A&A, 700, A117 (2025)
https://doi.org/10.1051/0004-6361/202555179

Astronomy & Astrophysics

Spatially resolved [CII]–gas conversion factor in early galaxies

L. Vallini[1,⋆], A. Pallottini[2,3], M. Kohandel[3], L. Sommovigo[4], A. Ferrara[3], M. Bethermin[5], R. Herrera-Camus[6,11], S. Carniani[3], A. Faisst[7], A. Zanella[1], F. Pozzi[8,1], M. Dessauges-Zavadsky[9], C. Gruppioni[1], E. Veraldi[10], and C. Accard[5]

[1] INAF, Osservatorio di Astrofisica e Scienza dello Spazio, Via P. Gobetti 93/3, I-40129 Bologna, Italy
[2] Università di Pisa, Dipartimento di Fisica "Enrico Fermi", Largo Bruno Pontecorvo 3, Pisa I-56127, Italy
[3] Scuola Normale Superiore, Piazza dei Cavalieri 7, I-56126 Pisa, Italy
[4] Center for Computational Astrophysics, Flatiron Institute, 162 Fifth Avenue, New York, NY 10010, USA
[5] Université de Strasbourg, CNRS, Observatoire Astronomique de Strasbourg, UMR 7550, 67000 Strasbourg, France
[6] Departamento de Astronomía, Universidad de Concepción, Barrio Universitario, Concepción, Chile
[7] Caltech/IPAC, 1200 E. California Blvd., Pasadena, CA 91125, USA
[8] University of Bologna, Department of Physics and Astronomy "Augusto Righi", Via Gobetti 93/2, I-40129 Bologna, Italy
[9] Département d'Astronomie, Université de Genève, Chemin Pegasi 51, 1290 Versoix, Switzerland
[10] Scuola Internazionale Superiore Studi Avanzati (SISSA), Physics Area, Via Bonomea 265, I-34136 Trieste, Italy
[11] Millenium Nucleus for Galaxies (MINGAL), Concepción, Chile

Received 16 April 2025 / Accepted 1 July 2025

ABSTRACT

Aims. Determining how efficiently gas collapses into stars at high redshifts is key to understanding galaxy evolution in the epoch of reionization (EoR). Globally, this process is quantified by the gas depletion time ($t_{\rm dep}$); on resolved scales, it is quantified by the slope and normalization of the Kennicutt-Schmidt (KS) relation. This work explores the global ($\alpha_{\rm [CII]}$) and spatially resolved ($W_{\rm [CII]}$) [CII]-to-gas conversion factors at high-z and their use when inferring gas masses, surface densities, and $t_{\rm dep}$ in the EoR.
Methods. We selected galaxies at $4 < z < 9$ from the SERRA cosmological zoom-in simulation, which features on-the-fly radiative transfer and resolves interstellar medium properties down to ≈30 pc. The [CII] emission modeling from photodissociation regions allows us to derive the global $\alpha_{\rm [CII]}$ and maps of $W_{\rm [CII]}$. We study their dependence on gas metallicity (Z), density (n), Mach number ($\mathcal{M}$), and burstiness parameter (κ_s), and provide best-fit relations.
Results. The $\alpha_{\rm [CII]}$ decreases with increasing Z and galaxy compactness, while the resolved $W_{\rm [CII]}$ shows two regimes: at $Z < 0.2\,Z_\odot$, it anticorrelates with n and Z but not with κ_s; above this threshold, it also depends on κ_s, with burstier regions having lower conversion factors. This implies $W_{\rm [CII]} \propto \Sigma_{\rm [CII]}^{-0.5}$, as dense, metal-rich, and bursty regions exhibit higher [CII] surface brightnesses. Applying a constant $\alpha_{\rm [CII]}$ leads to an overestimation of $\Sigma_{\rm gas}$ in bright $\Sigma_{\rm [CII]}$ patches; this in turn flattens the KS slope and leads to overestimations of $t_{\rm dep}$ by up to a factor of 4.

Key words. galaxies: evolution – galaxies: high-redshift – galaxies: ISM – early Universe

1. Introduction

The *James Webb* Space Telescope (JWST) has revealed an unexpected abundance of UV-luminous, massive galaxies in the epoch of reionization (EoR; e.g., Naidu et al. 2022; Finkelstein et al. 2022, 2024; Castellano et al. 2023; Arrabal Haro et al. 2023; Tacchella et al. 2023; Adams et al. 2024; Donnan et al. 2024; Carniani et al. 2024), challenging our understanding of early star formation and galaxy evolution. The high stellar masses, high number densities, and blue colors of newly discovered sources do not easily fit within pre-JWST frameworks; hence, new models have been proposed to explain these results. Leaving aside modifications of Λ cold dark matter (e.g., Padmanabhan & Loeb 2023; Matteri et al. 2025a,b), attempts have included enhanced star formation efficiency due to delayed feedback (Dekel et al. 2023; Li et al. 2024), a top-heavy initial mass function (e.g., Hutter et al. 2025; Trinca et al. 2024), dust removal driven by radiation-driven outflows that reduce the impact of dust on UV attenuation (Ferrara et al. 2023; Ferrara 2024), and stochastic variations in galaxy luminosity caused by bursty star formation (e.g., Pallottini & Ferrara 2023; Sun et al. 2023; Mirocha & Furlanetto 2023; Nikolić et al. 2024).

Most of these scenarios are linked to how quickly gas is converted into stars as quantified by the depletion time ($t_{\rm dep} = M_{\rm gas}/{\rm SFR}$). Deriving the cold gas mass ($M_{\rm gas}$) that fuels star formation in high-z galaxies, and their star formation rates (SFRs), is thus of utmost importance. A powerful tracer of the cold gas that eventually collapses to form stars is the fine-structure transition of ionized carbon (C^+) at 158 μm ([CII]). This is the brightest line in the rest-frame far-infrared (FIR) and, although up to ≈10%–20% of the flux can originate from diffuse ionized gas (Croxall et al. 2017), it predominantly traces the diffuse cold neutral medium ($T \approx 50$–100 K; Wolfire et al. 2003) and dense photodissociation regions (PDRs; Wolfire et al. 2022) that make up the external layers of giant molecular clouds (GMCs). Since the advent of the Atacama Large Millimeter Array (ALMA), the [CII] 158 μm line has been detected both in large galaxy samples (see Béthermin et al. 2020; Faisst et al. 2020 for ALPINE, Bouwens et al. 2022 for REBELS, and Herrera-Camus et al. 2025 for CRISTAL surveys) and in targeted sources (e.g., Maiolino et al. 2015; Capak et al. 2015; Knudsen et al. 2016; Carniani et al. 2018; Matthee et al. 2019; Glazer et al. 2024) in the EoR.

⋆ Corresponding author: livia.vallini@inaf.it

Interestingly, JWST-selected sources, with spectroscopic redshifts $z > 10$, remain elusive in [CII] observations, with only upper limits obtained so far (Fudamoto et al. 2024; Schouws et al. 2025). While overly short observing times can be an issue (Kohandel et al. 2024), another plausible possibility is the rapid exhaustion of cold gas in their interstellar medium (ISM) thanks to vigorous bursts of star formation (Witstok et al. 2025). Precisely determining $t_{\rm dep}$ is thus critical, but this relies on the adopted [CII]-to-$M_{\rm gas}$ conversion factor ($\alpha_{\rm [CII]} \equiv M_{\rm gas}/L_{\rm [CII]}$), which introduces systematic uncertainties in $M_{\rm gas}$[1] estimates (Sommovigo et al. 2021; Mitsuhashi et al. 2025; Algera et al. 2025). Zanella et al. (2018) first proposed [CII] as an alternative to the less luminous CO to pin down molecular gas in high-z sources (see Wolfire et al. 2010; Pineda et al. 2014, for low-z sources), finding $\alpha_{\rm [CII]} = (31\,{\rm M_\odot\,L_\odot^{-1}})$. Other studies report a wide range of values, from $\alpha_{\rm [CII]} \approx 72\,{\rm M_\odot\,L_\odot^{-1}}$ for local metal-poor dwarf galaxies (Madden et al. 2020, but see also Ramambason et al. 2024) to significantly lower values ($\alpha_{\rm [CII]} \approx 5{-}10\,{\rm M_\odot\,L_\odot^{-1}}$) in gravitationally lensed dusty star-forming galaxies at $z \sim 4.5$ (Rizzo et al. 2021) and quasars at $z \approx 6{-}7$ (Kaasinen et al. 2024; Salvestrini et al. 2025). At $z \approx 4{-}5.5$, Dessauges-Zavadsky et al. (2020) find agreement between the dynamical mass of galaxies in ALPINE and that inferred from [CII] adopting the Zanella et al. (2018) conversion factor; this is further evidence that [CII] is a total cold gas mass tracer (see also Heintz et al. 2021, who focus on HI).

We are living in an era when JWST and ALMA can spatially resolve EoR galaxies in both the rest-frame optical/UV (e.g., Übler et al. 2023; Tripodi et al. 2024; Venturi et al. 2024; Jones et al. 2024) and the FIR (e.g., Witstok et al. 2022; Posses et al. 2023; Vallini et al. 2024; Ikeda et al. 2025; Solimano et al. 2024). As a result, it is now possible to measure the resolved Kennicutt–Schmidt (KS) relation; ($\Sigma_{\rm SFR} \propto \kappa_s \Sigma_{\rm gas}^{1.4}$ Schmidt 1959; Kennicutt 1998) and thereby constrain the local gas depletion time ($t_{\rm dep} = \Sigma_{\rm gas}/\Sigma_{\rm SFR} \propto 1/\kappa_s$). The depletion time is inversely proportional to the so-called burstiness parameter (first introduced by Ferrara et al. 2019), namely the offset (κ_s) from the KS relation. Crucially, it remains unclear whether using a single $\alpha_{\rm [CII]}$ for different sub-kiloparsec regions in the ISM of high-z sources provides an accurate determination of the gas surface density ($\Sigma_{\rm gas}$) from the [CII] 158 μm surface brightness ($\Sigma_{\rm [CII]}$; e.g., Béthermin et al. 2023; Vallini et al. 2024; Accard, in prep.). Sub-kiloparsec variations in metallicity, density, and turbulence can significantly impact [CII] emission (e.g., Vallini et al. 2015; Ferrara et al. 2019; Pallottini et al. 2019; Herrera-Camus et al. 2021; Veraldi et al. 2025); a spatially resolved conversion factor, $W_{\rm [CII]} \equiv \Sigma_{\rm gas}/\Sigma_{\rm [CII]}$, is thus likely required.

This work aims to theoretically shed light on the connection between $W_{\rm [CII]}$ and the underlying ISM conditions in early galaxies, and on the relation between $W_{\rm [CII]}$ and $\alpha_{\rm [CII]}$. Theoretical works focusing on the [CII] emission both from resolved GMCs in the local Universe (Ebagezio et al. 2023; Gurman et al. 2024) and from galaxies in the EoR (Vallini et al. 2015; Olsen et al. 2017; Lagache et al. 2018; Vizgan et al. 2022; Casavecchia et al. 2025) have gained significant traction over the past decade. Among the many approaches, cosmological zoom-in simulations that feature on-the-fly radiative transfer and resolve ≈10 pc scales to accurately model [CII] emission from diffuse neutral gas, PDRs, and GMCs (e.g., Katz et al. 2017, 2022; Lupi & Bovino 2020; Pallottini et al. 2019, 2022; Schimek et al. 2024) are the most advanced tools for studying the ISM properties of high-redshift galaxies while retaining the cosmological context. In this study, we exploited the state-of-the-art SERRA cosmological zoom-in simulations (Pallottini et al. 2022).

The paper is structured as follows: In Sect. 2 we briefly describe SERRA, the [CII] emission model, and the sample of galaxies considered in this work. In Sects. 3 and 4 we present our results regarding $\alpha_{\rm [CII]}$, $W_{\rm [CII]}$, and their connection with the ISM properties. In Sect. 5 we discuss the observational implications for the derivation of the total cold gas mass, the $t_{\rm dep}$, and the KS relation. The conclusions are outlined in Sect. 6.

2. SERRA simulation

2.1. Galaxy formation and evolution

The SERRA simulation suite investigates the processes driving galaxies' formation and evolution during the EoR (Pallottini et al. 2022). SERRA uses a tailored version of the adaptive mesh refinement code RAMSES (Teyssier 2002) to evolve gas and dark matter (DM). The simulations start from $z = 100$, where initial conditions are generated with MUSIC (Hahn & Abel 2011), in a cosmological volume of $(20\,{\rm Mpc/h})^3$. RAMSES is used to track the evolution of DM, stars, and gas, reaching a baryon mass resolution of $1.2 \times 10^4\,{\rm M_\odot}$ and spatial resolution of ≈30 pc at $z \approx 6$ in the zoom-in regions, i.e., about the mass and size of typical GMCs (Federrath & Klessen 2013).

The chemical evolution is handled with KROME (Grassi et al. 2014), which solves a nonequilibrium chemical network encompassing species such as H, H^+, H^-, He, He^+, He^{++}, H_2, H_2^+, electrons, and metals, with roughly 40 reactions (Bovino et al. 2016; Pallottini et al. 2017a). Metallicity (Z) is tracked by summing heavy elements under the assumption of solar abundance ratios for metal species (Asplund et al. 2009). Dust scales with Z as $\mathcal{D} = Z\mathcal{D}_\odot$, where $\mathcal{D}_\odot = 0.3$ is the dust to metal ratio at solar metallicity (Rémy-Ruyer et al. 2014). SERRA also adopts a Milky Way-like dust composition and grain size distribution (Weingartner & Draine 2001). Star formation follows a KS-like relation (Schmidt 1959; Kennicutt 1998), with H_2 being the primary fuel for star formation (Pallottini et al. 2017a). The H_2 density is obtained from the nonequilibrium chemical network and, taking the photo-dissociation produced by the Lyman–Werner flux into account, computed on the fly (Pallottini et al. 2019). Lupi et al. (2020) show that adopting the same initial conditions but a star formation recipe based on the local gas turbulence results in differences in the stellar mass build-up only during the first ≈100 Myr of evolution. In this case the SFR history is more prone to bursts, and it depends on the stellar feedback adopted (see also Pallottini et al. 2025). Stars inject metals, radiation, and mechanical energy (Pallottini et al. 2017b). SERRA treats feedback in both thermal and turbulent forms: thermal energy cools via KROME-modeled thermo-chemical evolution, while turbulent energy dissipates over an eddy turnover timescale (Mac Low & Ferrara 1999). Finally, the interstellar radiation field is coupled with the chemical processes (Pallottini et al. 2019) and evolves dynamically with five frequency bins; it is solved on the fly using the moment-based radiative transfer module in RAMSES-RT (Rosdahl et al. 2013). The first two bins cover the Habing (1968) band (6.0–13.6 eV), with the second bin being specific for the Lyman–Werner radiation (11.2–13.6 eV),

[1] In this paper we adopt $\alpha_{\rm [CII]}$ as the total cold gas conversion factor without distinguishing between molecular and atomic. As detailed in Sect. 2.2, the [CII] emission is indeed computed accounting for both the outer PDR layer and the fully molecular clumps within molecular clouds.

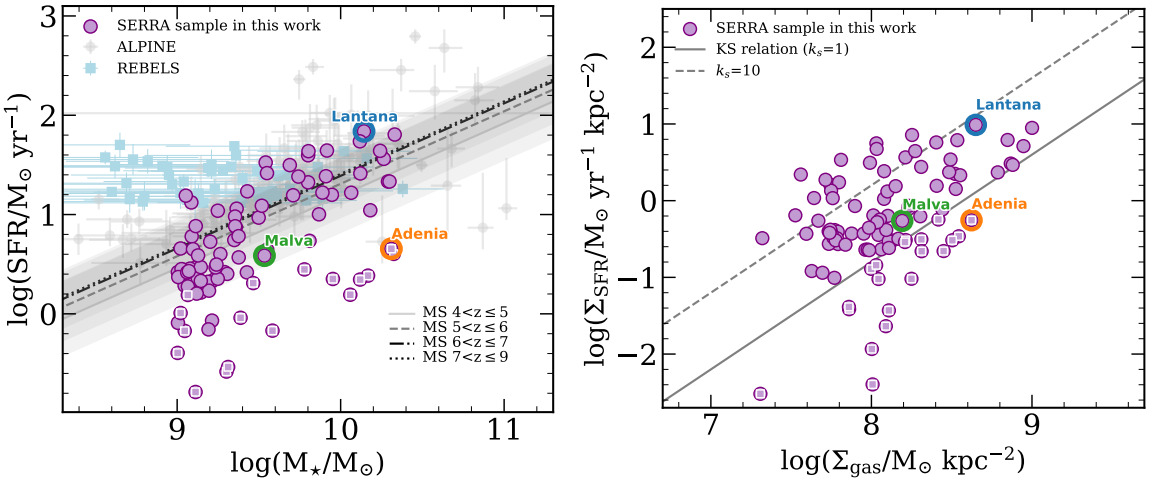

Fig. 1. Left panel: SFR vs. $M_\star$ relation for the SERRA sample (purple points), along with the MS parametrization in the CEERS sample in different redshift bins (gray lines), with their 1σ scatter (gray shaded areas) for 100 Myr-averaged SFRs (Cole et al. 2025). The SFR vs. $M_\star$ relations of ALPINE (Khusanova et al. 2021, gray points) and REBELS (Inami et al. 2022; Topping et al. 2022, light blue squares) are also plotted for comparison. Right panel: $\Sigma_{\rm SFR}$ vs. $\Sigma_{\rm gas}$ KS relation for the SERRA galaxies. The local KS relation is plotted with a solid gray line, and that obtained for burstiness parameter $\kappa_s = 10$ with a dashed gray line. Those sources that were below the KS relation (points with a white inner square) also fall below the MS. In both plots we highlight the three example galaxies discussed in Sect. 3 and whose cutouts are presented in Fig. 2.

which can photo-dissociate H_2. The remaining three bins cover the H-ionizing photons up to the first ionization level of He (13.6–24.59 eV). Further details can be found in Pallottini et al. (2019).

2.2. [CII] emission

The [CII] emission[2] is computed on a cell-by-cell basis using grids of CLOUDY models (Ferland et al. 2017). In SERRA, both species-by-species abundances and the line emission are post-processed to improve the precision of the prediction, at the cost of losing track of nonequilibrium effects. The opposite approach – adopting the chemistry from the simulation for line predictions at the cost of precision – is possible, and shows very little difference for the [CII] (see Lupi et al. 2020).

The Cloudy models used for the post processing account for variations in density, metallicity, and radiation field intensity, with the column density ($N_{\rm H}$) serving as the stopping criterion for the calculations. The PDR ($N_{\rm H} \approx 10^{21.5}\,{\rm cm^{-2}}$) and molecular layers ($N_{\rm H} \approx 10^{22.5}\,{\rm cm^{-2}}$) are fully sampled in the calculations. The spectral energy distribution used for the radiation field incident on the gas slab in CLOUDY assume a 10 Myr old STARBURST99 (Leitherer et al. 1999) stellar population. We have two identical grids of Cloudy models, in which the impinging spectral energy distribution includes – does not include – ionizing radiation ($h\nu > 13.6$ eV). Each grid, equally spaced in log scale, comprises 17 density bins ($10^{-2} \le n/{\rm cm^{-3}} \le 10^{6.5}$), 8 metallicity bins ($10^{-3} \le Z/Z \le 10^{0.5}$), and 12 interstellar radiation field intensity bins ($10^{-1} \le G/G_0 \le 10^{4.5}$, with $G_0 = 1.6 \times 10^{-3}\,{\rm erg\,s^{-1}\,cm^{-2}}$ in the $6 \le h\nu < 13.6$ eV (Habing 1968 band), resulting in 1632 models. Due to the ∼30 pc resolution of SERRA, dense H II regions, GMCs, and PDRs remain unresolved and require a sub-grid treatment (see Decataldo et al. 2017; Vallini et al. 2018; Pallottini et al. 2019). [CII] emission is computed using the Cloudy grids outlined above, interpolated over G_0, $N_{\rm H}$, and Z in the cell. We adopted Cloudy models with ionizing radiation either if the HII region is resolved on the fly in the simulation or if young ($t_\star < 10$ Myr) stars are contained the gas cell. If such conditions are not met, the radiation is treated as non-ionizing. For the interpolation in gas density, we accounted for the log-normal density distribution within each cell following the approach described in Vallini et al. (2018): the sub-grid density probability density function (PDF) was parametrized as a function of the local Mach number ($\mathcal{M}$), defined as the ratio of the turbulent plus thermal velocities over the turbulent velocity. The results of the CLOUDY postprocessing are spatially resolved maps and hyperspectral data cubes (HSDCs), which provide line spectra in position–position–velocity space (Kohandel et al. 2020, 2024). For optically thin lines, such as the [CII] 158 μm, the luminosity is the sum of the emission cells within the HSDC centered on each galaxy and with side of 5 kpc.

2.3. Sample selection

We started from a parent sample of 3218 SERRA galaxies ($10^8\,{\rm M_\odot} < M_\star < 10^{10.3}\,{\rm M_\odot}$), whose kinematic properties in both [CII] and Hα were analyzed in Kohandel et al. (2024). For this work, we selected a subsample of 98 sources with stellar masses $M_\star > 10^9\,{\rm M_\odot}$ in the redshift range $4.0 \le z \le 8.9$. Our sample includes galaxies with SFR = 0.01−70 $\rm M_\odot\,yr^{-1}$. The SFR is averaged over the last 30 Myr. In Fig. 1 we show the location of our sources in the SFR–$M_\star$ and $\Sigma_{\rm gas}$–$\Sigma_{\rm SFR}$ planes. In the former, the galaxies broadly follow the star formation main sequence (MS), although defining the MS is not straightforward for sources with bursty star formation (Gelli et al. 2025), particularly considering its evolution across a broad range of redshifts. In Fig. 1 we report the Cole et al. (2025) parametrization of the MS in different redshift bins encompassing redshift range of our sample. From Fig. 1, it is clear that overall, SERRA sources are scattered along and below the Cole et al. (2025) MS parametrizations. For comparison we also report the location of the two largest [CII] detected samples at high-z: ALPINE (see Khusanova et al. 2021), and REBELS (see Inami et al. 2022; Topping et al. 2022).

In the right panel of Fig. 1 the major fraction of our galaxies lie on and above the local KS relation (Heiderman et al. 2010;

[2] Several other emission lines, besides [CII], are computed in SERRA, both in the rest-frame FIR and in the optical.

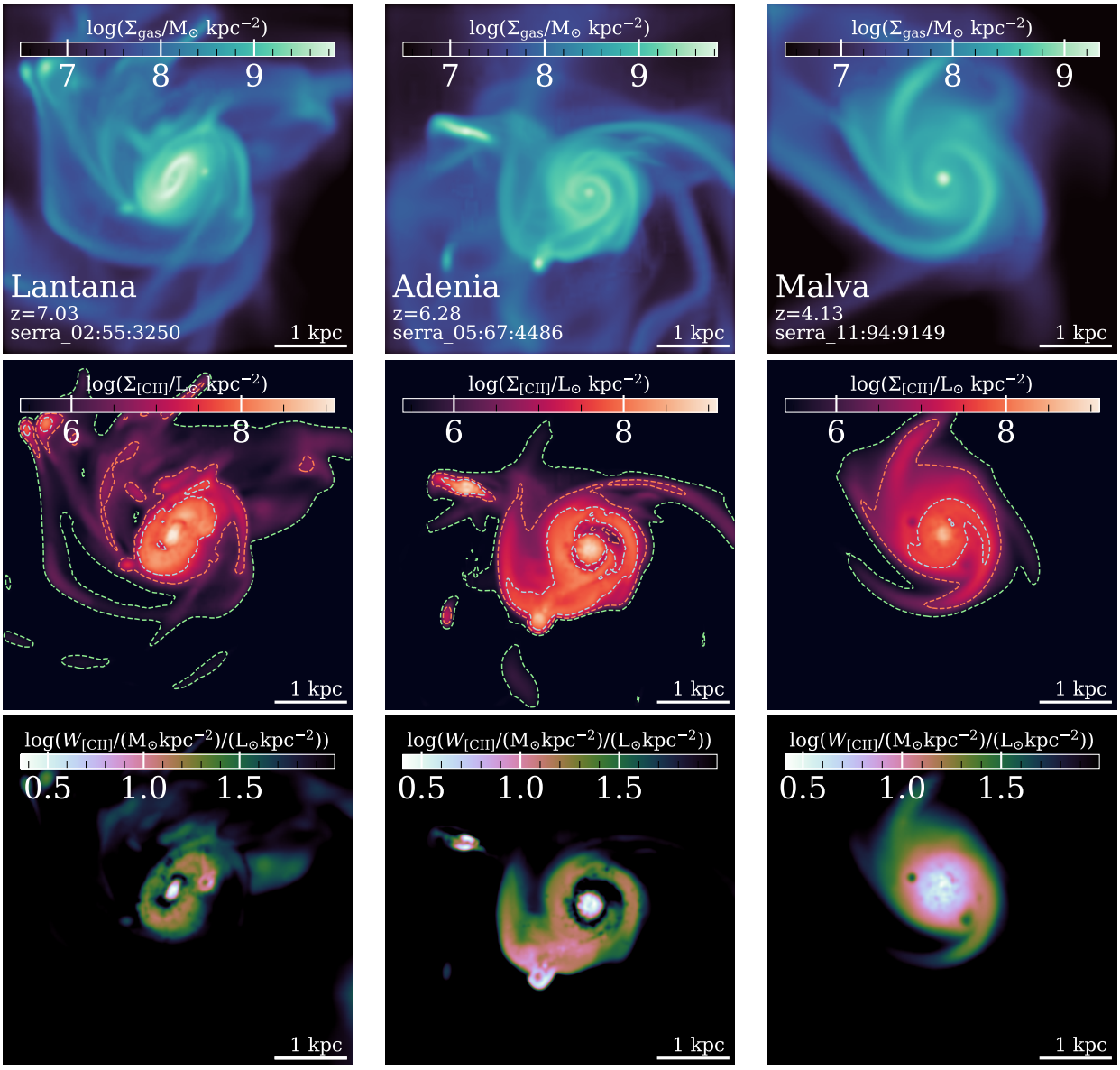

Fig. 2. Cutouts of $5 \times 5\,\mathrm{kpc}^2$ size centered on three SERRA galaxies. From left to right: Lantana (`serra02:55:3350`, $z \approx 7.0$), Adenia (`serra05:67:4486`, $z \approx 6.3$), and Malva (`serra11:94:9149`, $z \approx 4.1$). From top to bottom: Gas surface density, [CII] surface brightness, and the spatially resolved conversion factor, $W_{[\mathrm{CII}]}$, in units of $[(\mathrm{M}_\odot\,\mathrm{kpc}^{-2})/(\mathrm{L}_\odot\,\mathrm{kpc}^{-2})]$. To guide the eye, dashed green, orange, and light blue lines in the $\Sigma_{[\mathrm{CII}]}$ maps highlight $\Sigma_{[\mathrm{CII}]} = 10^{5.5}$, $10^{6.5}$, and $10^{7.5}\,\mathrm{L}_\odot\,\mathrm{kpc}^{-2}$, respectively.

de los Reyes & Kennicutt 2019) by a factor of up to $\kappa_s \approx 10$ (see also Pallottini et al. 2022). Finally, we note that the sources below the MS are also below the local KS relation. These galaxies are experiencing quenching in star formation over the last 30 Myr, yet their gas is still not completely exhausted ($\Sigma_{\mathrm{gas}} \gtrsim 10^8\,\mathrm{M}_\odot\,\mathrm{kpc}^{-2}$). How this translates into the [CII]-to-M_{gas} conversion factor is addressed in the next sections.

3. The global $\alpha_{[\mathrm{CII}]}$ conversion factor in SERRA

The $\alpha_{[\mathrm{CII}]} = M_{\mathrm{gas}}/L_{[\mathrm{CII}]}$ (in units of $\mathrm{M}_\odot\,\mathrm{L}_\odot^{-1}$) is computed from the M_{gas} and $L_{[\mathrm{CII}]}$ obtained by integrating the gas surface density, Σ_{gas}, and the [CII] surface brightness, $\Sigma_{[\mathrm{CII}]}$, within a $5\times5\,\mathrm{kpc}^2$ field of view centered on each simulated galaxy, which is obtained by collapsing (i.e., projecting in 2D) the HSDCs.

In Fig. 2 we show example cutouts of Σ_{gas}, and $\Sigma_{[\mathrm{CII}]}$ for three sources spanning redshifts from well within the EoR (Lantana, `serra02:55:3350`, at $z = 7.03$) to the end of reionization (Adenia, `serra05:67:4486`, at $z = 6.28$), and half a gigayear after the EoR (Malva, `serra11:94:9149` at $z = 4.13$).

The mean conversion factor in the SERRA sample is $\log(\alpha_{[\mathrm{CII}]}/\mathrm{M}_\odot\,\mathrm{L}_\odot^{-1}) = 1.28$ ($\sigma = \pm0.2$ dex) and falls within the range bracketed by previous estimates in the literature. We first explored $\alpha_{[\mathrm{CII}]}$–redshift, $\alpha_{[\mathrm{CII}]}$–$M_\star$, and $\alpha_{[\mathrm{CII}]}$–Δ_{MS} (deviation from the MS) correlations. Our aim is to test whether the observational results from Zanella et al. (2018), which indicate $\alpha_{[\mathrm{CII}]}$ does not significantly depend on any of these quantities up to $z \approx 2$, also hold for the SERRA galaxies up to $z \approx 9$. To quantify the presence (or lack thereof) of correlations, we performed a Spearman's test, finding rank correlation coefficients $r_s = 0.3$, 0.07, 0.09 and corresponding p-values 0.002, 0.47, 0.37 for

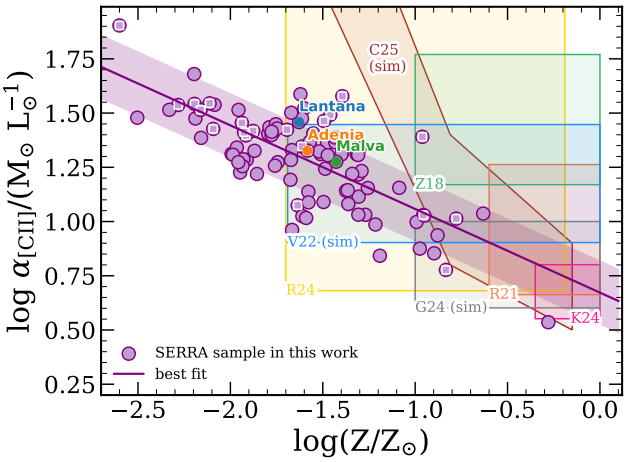

Fig. 3. $\alpha_{[CII]}$ vs. $\log Z$ for the SERRA galaxies (purple points, with inner white squares if they fall below the local KS relation) along with the best-fit linear regression $\pm1\sigma$ dispersion (purple line and shaded area). Lantana, Adenia, and Malva are plotted in blue, orange, and green, respectively. Previous derivations of $\alpha_{[CII]}$ in the literature are shown with shaded areas as follows: the green shaded area represents the Zanella et al. (2018) results ($\log\alpha_{[CII]} = 1.5$ with 0.3 dex dispersion over $\log(Z/Z_\odot) \approx [-1, 0.0]$); the yellow shaded area the Ramambason et al. (2024) results (converted into $M_\odot\,L_\odot^{-1}$ units, over $\log(Z/Z_\odot) \approx [-1.69, -0.3]$ range); the orange shaded area the Rizzo et al. (2021) results ($\log\alpha_{[CII]} = [0.66, 1.3]$ assuming a fiducial range $\log(Z/Z_\odot) \approx [-0.5, 0.0]$ for the dusty star-forming galaxies in the sample); and the pink shaded box the results from Kaasinen et al. (2024), who report $\alpha_{[CII]} = 4.6 \pm 1.6\times$ lower than Zanella et al. (2018), over $\log(Z/Z_\odot) \approx [-0.3, 0.0]$ for the quasi-stellar objects in their sample. Cosmological and single cloud simulations (labeled "sim") from Vizgan et al. (2022) and Gurman et al. (2024) are almost constant within their Z range, and are plotted in blue and gray, respectively. The $\alpha_{[CII]}$–$Z_\star$ relation from Casavecchia et al. (2025) is shown in brown.

redshift, $\log M_\star$, and $\log\Delta_{MS}$[3], respectively. Overall, we recover a very weak, marginally significant correlation with z, while the $\alpha_{[CII]}$ versus $M_\star$, and $\alpha_{[CII]}$ versus Δ_{MS} do not show any statistically significant correlation, in agreement with Zanella et al. (2018, see also Accurso et al. 2017; Zhao et al. 2024). The interested reader can find the plots in Fig. A.1.

The situation is markedly different in the $\alpha_{[CII]}$–Z plane (Fig. 3), where we find a significant negative correlation ($r_s = -0.65$, p-value $= 5.1\times10^{-13}$) between $\alpha_{[CII]}$ and Z. We compare the SERRA trend with previous observational results spanning different metallicity ranges, as indicated by the shaded areas in Fig. 3. In low-metallicity dwarf galaxies ($\log(Z/Z_\odot) \approx [-1.69, -0.3]$), Ramambason et al. (2024) reported a median $\alpha_{[CII]} \approx 48\,M_\odot/L_\odot$, while the canonical value from Zanella et al. (2018), $\alpha_{[CII]} = 31\,M_\odot/L_\odot$, corresponds to sources with $\log(Z/Z_\odot) \approx [-1, 0]$. This appears somewhat in tension with our findings, as we measure $\alpha_{[CII]} \approx 5$–10 in the 0.5–$1\,Z_\odot$ range. SERRA values are instead consistent with the $\alpha_{[CII]} \approx 4$–$7.5\,M_\odot/L_\odot$ reported by Rizzo et al. (2021) and Kaasinen et al. (2024) for dusty star-forming and quasar host galaxies. While the metallicity of those sources is not well constrained, we adopted a fiducial $\log(Z/Z_\odot) \approx [-0.3, 0.0]$.

In Fig. 3 we also compare the SERRA results with both large-scale cosmological simulations (Vizgan et al. 2022; Casavecchia et al. 2025) and GMC-scale simulations that incorporate nonequilibrium chemistry (Gurman et al. 2024). Vizgan et al. (2022) post-processed SIMBA simulations with SIGAME (Olsen et al. 2017), finding $\alpha_{[CII]} \approx 18\,M_\odot/L_\odot$ in galaxies at $z \approx 6$, which is in line with our results, albeit for galaxies with lower stellar masses. Note that they reported a very weak correlation with Z, in contrast to the significant negative correlation we find. Casavecchia et al. (2025), using the COLD-SIM simulations, obtained a redshift-dependent molecular gas mass–to–[CII] luminosity relation. When extrapolated to match the median redshift and [CII] luminosity of the SERRA sample, their relation suggests $\alpha_{[CII]} \approx 28\,M_\odot/L_\odot$. Casavecchia et al. (2025) also report a negative correlation between $\alpha_{[CII]}$ and stellar metallicity in their simulation, as highlighted by the shaded C25 area in Fig. 3. The $\alpha_{[CII]}$ values in SERRA are broadly consistent with those from GMC-scale simulations by Gurman et al. (2024), which span $Z \approx 0.1$–$1\,Z_\odot$. This supports the idea that radiative transfer and ISM properties on sub-parsec scales must be considered, as they significantly impact the accuracy of [CII] emission predictions. Finally, an important caveat to be emphasized is that metallicity in SERRA is derived directly from the O/H ratio in each cell, then converted to solar units using Asplund et al. (2009). In contrast, observational estimates of Z rely on calibrations based on emission line ratios (see Pallottini et al. 2025). A dedicated study comparing Z derived from these calibrations with the intrinsic O/H values in SERRA is deferred to future work.

The linear regression fit to our simulated sources is given by

$$\log(\alpha_{[CII]}/M_\odot\,L_\odot^{-1}) = -0.39\log(Z/Z_\odot) + 0.67 \quad (1)$$

with a dispersion of 0.14 dex. The errors on the best-fit parameters are summarized in Table 1. Interestingly, we note that the anticorrelation of $\alpha_{[CII]}$ with metallicity mirrors the well-known anticorrelation of the CO-to-H_2 conversion factor with Z ($\alpha_{CO} \propto Z^{-0.5}$; Bolatto et al. 2013; Narayanan et al. 2011). At low Z, the reduced dust shielding allows UV radiation to penetrate deeper into GMCs, leading to CO photodissociation and to a drop in the CO luminosity efficiency, thus boosting α_{CO}. Likewise, to understand the $\alpha_{[CII]}$–Z anticorrelation, we must focus on PDRs and GMCs and hence on the spatially resolved $W_{[CII]}$.

4. Spatially resolved $W_{[CII]}$ conversion factor

By leveraging the detailed physical information of SERRA galaxies on ≈30 pc scales, we turned to study how local conditions influence the conversion factor. In Fig. 2 we show the map of $W_{[CII]} = \Sigma_{gas}/\Sigma_{[CII]}$ for Lantana, Adenia, and Malva. By visually inspecting the maps, we note that the spatially resolved conversion factor shows a clear radial decline, decreasing from the periphery toward the center of the sources, where Z, n, and $\mathcal{M}$ are higher. The radial behavior of $W_{[CII]}$ resembles that derived in PHANGS (Physics at High Angular resolution in Nearby GalaxieS) (see, e.g., Sandstrom et al. 2013; Leroy et al. 2025) for the CO-to-H_2 at $z = 0$, where the central high surface and volume density regions of local galaxies are characterized by low α_{CO}. To separately quantify the impact of gas metallicity, density, and turbulence on the $W_{[CII]}$, in Fig. 4 we plot the 2D mass-weighted and [CII]-weighted kernel density estimates (KDEs) of $W_{[CII]}$ as a function of the spatially resolved (pixel by pixel) Z, n, and Mach number $\mathcal{M}$ for Lantana, Adenia, and Malva. We find a clear anticorrelation between the conversion factor with each of these three quantities, albeit for Adenia we obtain a larger scatter than for the other two galaxies; this is due to the fact that Adenia is caught after a major merger (Rizzo et al. 2022). Overall,

[3] We adopted the MS by Cole et al. (2025) in the corresponding redshift bin of each SERRA galaxy.

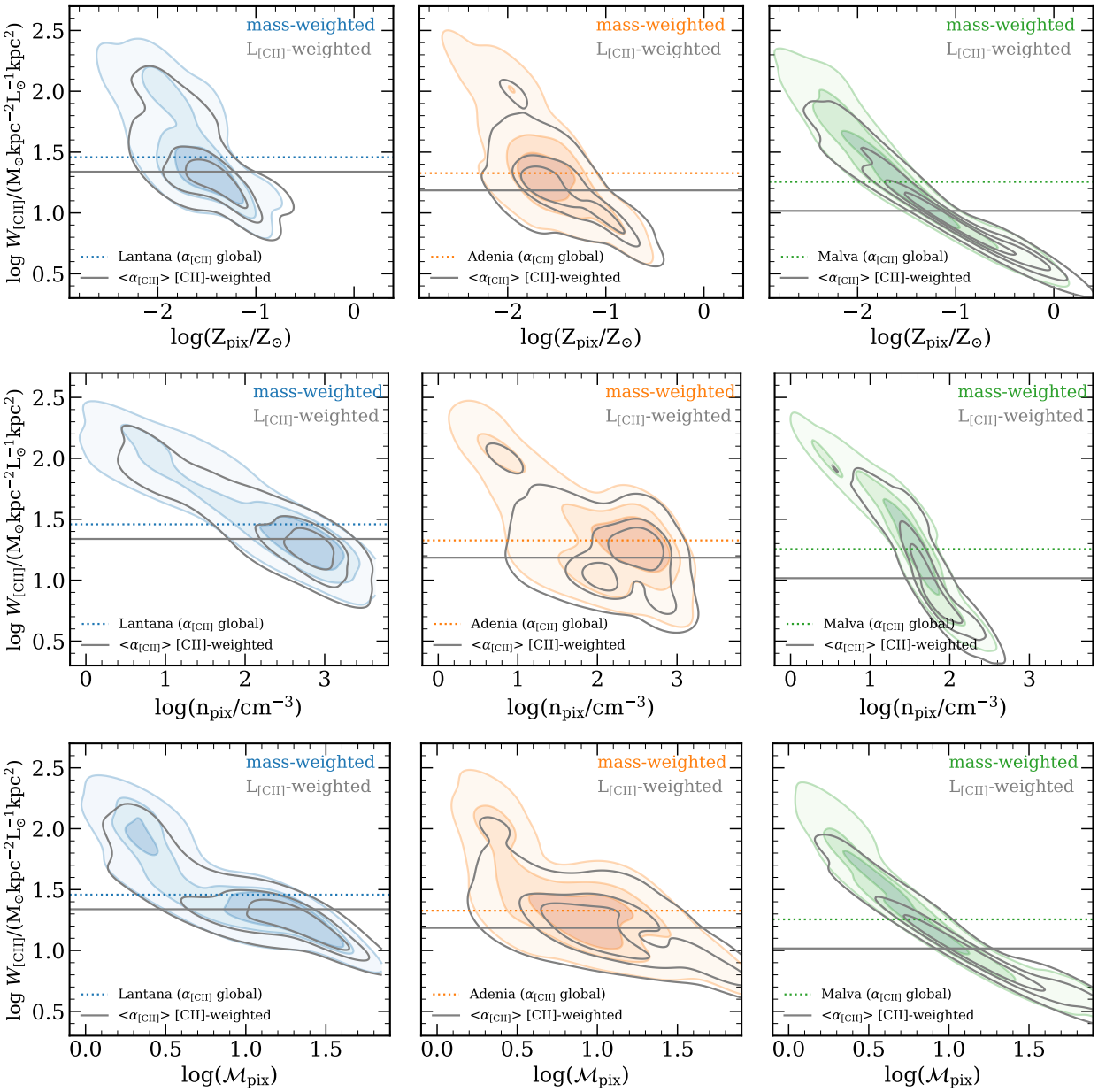

Fig. 4. Spatially resolved conversion factor ($W_{[CII]}$) as a function of different physical properties within 30 pc size pixels in the ISM of the three galaxies shown in Fig. 2. We show the mass-weighted KDE of pixels in the $W_{[CII]}$–Z plane (top row), $W_{[CII]}$–n plane (middle row), and $W_{[CII]}$–$\mathcal{M}$ plane (bottom row) for Lantana (z = 7.03, left), Adenia (z = 6.28, center), and Malva (z = 4.13, right). In each panel, we also show the [CII]-weighted KDEs with gray contours. The global ([CII]-weighted) value of $\alpha_{[CII]}$ for each galaxy is reported with a dashed (solid) line.

the highest-redshift galaxy, Lantana, having the lowest metallicity and a plume of patches in its ISM with low ($\log \mathcal{M} \approx 0.3$) Mach number, has marginally higher $\alpha_{[CII]}$. We further note that the mass-weighted and [CII]-weighted KDEs closely match each other, albeit the [CII]-weighted ones do not show up at the high end of the $W_{[CII]}$ range. These large $W_{[CII]}$ values correspond to patches of the ISM that are intrinsically [CII] faint because they are characterized by low-density ($\log(n/\mathrm{cm}^{-3}) \leq 0.5$) and low metallicity ($\log(Z/Z_\odot) \leq -2$). These high $W_{[CII]}$ plumes account for <15% of the total gas mass in every galaxy.

4.1. A physical intuition on how ISM properties shape $W_{[CII]}$

To gain a physical intuition on how the ISM properties shape $W_{[CII]} = \Sigma_{gas}/\Sigma_{[CII]}$, we exploited the [CII] emission model presented in Ferrara et al. (2019, F19 hereafter) that isolates three key properties impacting $\Sigma_{[CII]}$: metallicity, density, and the galaxy burstiness. F19 enables the computation of the surface brightness of [CII] from the ionized and the PDR layers of a gas slab illuminated by UV radiation from newly formed stars. The surface brightness is determined as the average gas density (n) of the HII and PDR environments – characterized by the electron density (n_e) and the neutral gas density (n_H), respectively[4] – the dust-to-gas ratio ($\mathcal{D} \propto Z$, where Z is the gas metallicity), and ionization parameter, U. The U can be expressed in terms of observed quantities by deriving its relation ($U \propto \Sigma_{SFR}/\Sigma_{gas}$;

[4] Both n_e and n_H can be expressed as a function of n. In the ionized layer, $n_e = x_e n \approx n$ assuming an ionized fraction $x_e \approx 1$, while in the PDR the neutral gas density $n_H = (1 - x_e)n \approx n$ given that $x_e \approx 0$.

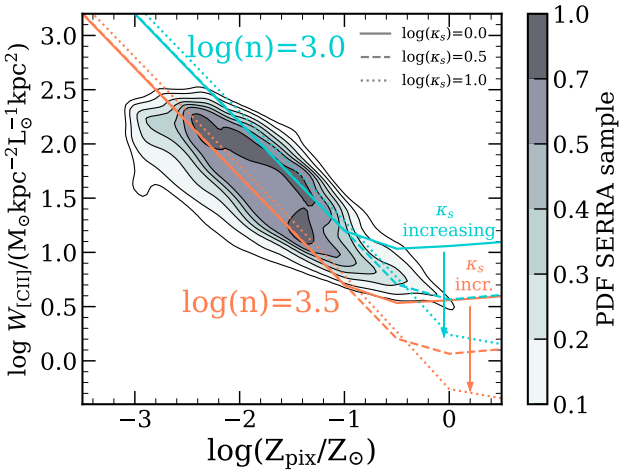

Fig. 5. 2D PDF of the spatially resolved conversion factor ($W_{[CII]}$) as a function of the spatially resolved metallicity (Z_{pix}) from the entire sample of SERRA sources. For comparison, we plot the theoretical estimates obtained with the F19 model assuming gas densities $\log(n/cm^{-3}) = 3$ (red) and $\log(n/cm^{-3}) = 3.5$ (cyan). We plot the results with burstiness parameters of $\log \kappa_s = 0$ (solid lines), $\log \kappa_s = 0.5$ (dashed lines), and $\log \kappa_s = 1.0$ (dotted lines).

see Eqs. 38 and 40 in F19). This leaves us with the κ_s parameter, which describes the burstiness of the galaxy.

In Fig. 5 we plot the $W_{[CII]}$ versus Z relation obtained by substituting the analytical equations for $\Sigma_{[CII]}$ by F19. We vary also the gas density ($\log(n/cm^{-3}) = 3, 3.5$, different colors), and the burstiness ($\log \kappa_s = 0, 0.5, 1$, different lines). It is worth noting that the critical density of the [CII] line emission is $\log(n_{crit}/cm^{-3}) = 3.3$ (Tielens 2005). In Fig. 5 we note two distinct regimes: one at low metallicities, where $W_{[CII]}$ depends on Z and n but not on κ_s, and the other one at high metallicities where instead $W_{[CII]}$ is modulated by κ_s and n, but is only weakly dependent on Z. The first regime ($Z < 0.2\,Z_\odot$) can be understood by noticing that the [CII] flux can be written as (see F19 for details)

$$\Sigma_{[CII]} \propto nZ\Sigma_{gas}. \tag{2}$$

Hence, given that $W_{[CII]} = \Sigma_{gas}/\Sigma_{[CII]}$, it follows that $W_{[CII]} \propto (1/nZ)$ with no dependence on κ_s. At fixed Z, $W_{[CII]}$ decreases with increasing n (see the different colored lines in Fig. 5).

In the high-metallicity regime ($Z \gtrsim 0.2\,Z_\odot$) instead, $W_{[CII]}$ reaches a constant value that depends on the burstiness. This can be understood by considering that, in this regime, $\Sigma_{[CII]}$ can be written as

$$\Sigma_{[CII]} \propto nZ \ln\left(1 + 10^5 wU\right), \tag{3}$$

with $w = (1 + 0.9Z^{1/2})^{-1}$. Consider that (i) U can be linked to the Σ_{SFR} and κ_s as

$$U \propto 10^{-3}\kappa_s^{10/7}\Sigma_{SFR}^{-3/7}, \tag{4}$$

and that (ii) Σ_{gas} can be expressed as a function of Σ_{SFR} and κ_s via the KS relation

$$\Sigma_{gas} = \left(\frac{\Sigma_{SFR}}{10^{-12}}\kappa_s\right)^{5/7}. \tag{5}$$

Thus, the final expression for $W_{[CII]}$ becomes

$$W_{[CII]} \propto \frac{\kappa_s^{-5/7}}{nZ\ln(1 + 10^2 w\kappa_s^{10/7})}, \tag{6}$$

assuming Σ_{SFR} is constant. At fixed Z and n, for small values of κ_s ($\kappa_s \approx 1$), the logarithm term is $\ln(1 + 10^2 w\kappa_s^{10/7}) \approx 10^2 w\kappa_s^{10/7}$, leading to

$$W_{[CII]} \sim \kappa_s^{-15/7}. \tag{7}$$

Thus, for small κ_s, $W_{[CII]}$ decreases as $\kappa_s^{-15/7}$. For large κ_s ($\kappa_s \approx 100$), the logarithm starts to be relevant, so the dominant scaling becomes

$$W_{[CII]} \sim \frac{\kappa_s^{-5/7}}{\ln \kappa_s}. \tag{8}$$

This implies a slower decrease in $W_{[CII]}$ with increasing κ_s. Overall, bursty regions are expected to exhibit lower $W_{[CII]}$ values because the [CII] emission per unit mass is higher. This occurs as the molecular region behind the PDR shifts toward higher column densities, making more gas effectively capable of emitting [CII]. The dependence on metallicity Z is still present as it is contained in both w and the denominator of $W_{[CII]}$. It is possible to show that in this regime

$$W_{[CII]} \sim \frac{1}{Z\ln(1 + 10^2 w\kappa_s^{10/7})}. \tag{9}$$

Thus, increasing Z causes $W_{[CII]}$ to decrease more slowly than a simple $1/Z$ dependence. Obviously, the [CII] luminosity depends also on the gas density. At fixed metallicity, higher gas densities shift $W_{[CII]}$ to lower values, consistent with theoretical expectations (see Fig. 5).

Very interestingly, the F19 model accurately captures the average properties of the SERRA sample, with the 2D PDF of the simulated $W_{[CII]}$–Z from all the pixels from all the galaxies in the sample nicely aligned with the theoretical lines. The turbulent and clumpy nature of the ISM is incorporated in SERRA by parameterizing the lognormal density distribution in each cell as a function of $\mathcal{M}$, which sets the dispersion $\sigma^2 \approx \ln(1 + \mathcal{M}^2)$ of the lognormal. The average Mach number in our sample is $\langle\mathcal{M}\rangle = 15$ (see also Pallottini et al. 2022). The resulting $n_{subgrid}$ is then used in the post-processing to compute the [CII] emission. Although a high-density power-law tail can develop due to self-gravity (Federrath & Klessen 2013; Girichidis et al. 2014) and affect tracers of denser gas, its impact on [CII] is expected to be minimal, as the critical density of [CII] ($\approx 10^3\,cm^{-3}$) is already well sampled by the lognormal distribution for $\mathcal{M} > 10$ (see Vallini et al. 2018). For the entire SERRA sample, the [CII]-weighted $\langle\log(n_{subgrid}/cm^{-3})\rangle = 3.1$ is in excellent agreement with the $\log(n/cm^{-3}) = [3.0, 3.5]$ lines from the F19 model. The [CII]-weighted average gas density (from the simulation without sub-grid implementation) is $\langle\log(n/cm^{-3})\rangle = 2.1$.

4.2. Best-fit equations for $W_{[CII]}$

With this physical intuition at hand, we next turned to the SERRA sample and searched for relations that are useful for inferring the conversion factor from spatially resolved observations of [CII]. For instance, an incorrect conversion factor might lead to a severe overestimate of Σ_{gas} in the center of galaxies where the metallicity, density, and burstiness are overall higher than at the periphery. Stated differently, $W_{[CII]}$ is expected to be overall lower than the global values.

To this aim, we considered our SERRA sample and derived the relation between $W_{[CII]}$, measured on $\approx$30 pc scales, and $\Sigma_{[CII]}$ for all the galaxies in our sample (Fig. 6). As expected, at fixed $\Sigma_{[CII]}$ the conversion factor increases for decreasing metallicity.

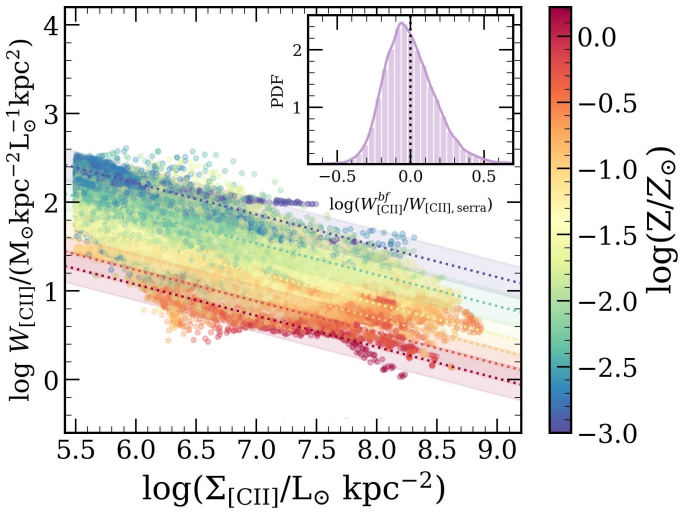

Fig. 6. Spatially resolved conversion ($W_{[CII]}$) factor as a function of the [CII] surface brightness ($\Sigma_{[CII]}$) within ≈30 pc size pixels (colored points) in the ISM of SERRA galaxies. The color-code reflects the metallicity within each pixel. The best-fit relation (dispersion) from Eq. (10), for different metallicities, is plotted with dotted lines (shaded areas), using the same color-code. The inset shows the PDF of the log error between the $W_{[CII]}$ obtained pixel by pixel using the best-fit relation and the actual one from the simulation.

Moreover, the brighter the $\Sigma_{[CII]}$ the lower is the conversion factor, indicating that brighter spots in the ISM of early galaxies correspond to denser PDRs, which are (see Fig. 5) characterized by lower conversion factors with respect to regions with comparable metallicity but lower density. Given that the sub-parsec density distribution in the ISM of high-z galaxies is difficult to derive observationally, we write a simplified, effective model that depends on $\Sigma_{[CII]}$ and Z:

$$\log(W_{[CII]}/\mathrm{M}_\odot\,\mathrm{kpc}^{-2}/\mathrm{L}_\odot\,\mathrm{kpc}^{-2}) = A\log\left(\frac{\Sigma_{[CII]}}{\mathrm{L}_\odot\,\mathrm{kpc}^{-2}}\right) + B\log\left(\frac{Z}{Z_\odot}\right) + C + \sigma, \quad (10)$$

where σ is a Gaussian noise term, quantifying the intrinsic scatter due to physical processes not explicitly captured by the metallicity nor the [CII] surface brightness.

We adopted a Bayesian framework and estimated the posterior distribution of the parameters A, B, C and the intrinsic scatter σ using a Markov chain Monte Carlo integrator (`emcee`; Foreman-Mackey et al. 2013, and references therein)[5]. We assumed flat priors $A < 0$, $B < 0$, and $\sigma > 0$. The resulting posteriors are $A = -0.355^{0.003}_{-0.017}$, $B = -0.324^{0.048}_{-0.004}$, $C = 3.37^{0.191}_{-0.026}$, and $\sigma = 0.184$. These are summarized in Table 1. Substituting the best-fit parameters in Eq. (10), the resulting relations (scatter) at fixed metallicity are plotted with lines and shaded areas in Fig. 6. We analyzed the PDF of the logarithmic error, defined as the difference between log $W_{[CII]}$ from the simulation and the value predicted by the best-fit equation (Eq. (10)). We find that this distribution mostly falls within ±0.5 dex, indicating that the model's predictions generally agree with the simulation within this margin of error. Finally, if the information of the spatially resolved metallicity is not available, in Table 1, we provide the parameters of the linear regression:

$$\log(W_{[CII]}/\mathrm{M}_\odot\,\mathrm{kpc}^{-2}/\mathrm{L}_\odot\,\mathrm{kpc}^{-2}) = A\log\left(\frac{\Sigma_{[CII]}}{\mathrm{L}_\odot\,\mathrm{kpc}^{-2}}\right) + C. \quad (11)$$

The important caveat is that the scatter around this relation, $\sigma = 0.4$, is wider than that obtained for the physical model (Eq. (10)), since the metallicity Z is not explicitly accounted for.

5. Discussion

5.1. Using $W_{[CII]}$ to derive the KS relation and t_{dep}

In the previous sections we have shown that the spatially resolved $W_{[CII]}$ exhibits a clear decreasing trend toward the central regions of galaxies, which correspond to the most actively star-forming, metal-enriched, and densest patches of their ISM. These regions are also characterized by the highest [CII] surface brightness, with which $W_{[CII]}$ anticorrelates (see Eq. (10)). In what follows, we quantify the bias introduced by using a fixed $\alpha_{[CII]}$ instead of $W_{[CII]}$ when determining the slope and normalization of the KS relation and the gas depletion time.

To do so, in Fig. 7 we start with the spatially resolved KS relation obtained from SERRA, considering $30\times30\,\mathrm{pc}^2$ pixels drawn from the entire sample. For each pixel, $\Sigma_{SFR,H\alpha}$ is derived from the Hα surface brightness using Kennicutt (1998), while Σ_{gas} is taken directly from the simulation. As shown by the color-coded shaded area in Fig. 7, the 2D PDF of all SERRA pixels aligns well with the KS relation, consistent with the standard ≈1.4 slope, with pixels characterized by burstiness parameters in the range $\kappa_s = 1-10$. However, if instead of using Σ_{gas} from the simulation we adopt a fixed $\alpha_{[CII]}$ (Zanella et al. 2018) to convert $\Sigma_{[CII]}$ into $\Sigma_{gas} = \alpha_{[CII]}\Sigma_{[CII]}$, the resulting KS relation becomes significantly flatter. This occurs because the gas surface density is overestimated in regions with high $\Sigma_{[CII]}$, highlighting a critical caveat when using spatially resolved [CII] observations to study the KS relation (see also Accard et al., in prep. for the ALPINE-CRISTAL sample). In contrast, when we apply our best-fit $W_{[CII]}-\Sigma_{[CII]}$ relation (Eq. (10)) to convert $\Sigma_{[CII]}$ into Σ_{gas}, we successfully recover the intrinsic KS relation from SERRA, reinforcing the validity of Eq. (10) and its use in spatially resolved observations, both at high-z and in the local Universe (see the recent Kovačić et al. 2025).

Furthermore, adopting a single conversion factor leads to an overestimation of the depletion time (t_{dep}) in bursty ISM regions and, consequently, across entire galaxies. This is depicted in the right panel of Fig. 7 where we plot the [CII] weighted PDF of the depletion times inferred pixel by pixels inverting the KS relation obtained with the three different approaches outlined before. While in the SERRA galaxies (labeled "ground truth" in Fig. 7) the average depletion time is $\langle t_{dep}\rangle \approx 0.1$ Gyr, when using the fixed conversion factor one would infer a four times longer depletion time, $\langle t_{dep}\rangle \approx 0.4$ Gyr.

5.2. The impact of compactness on the global $\alpha_{[CII]}$

As discussed in Sect. 4.1, $W_{[CII]}$ anticorrelates with n, Z, and burstiness parameter κ_s. Given that these properties also drive an increase in $\Sigma_{[CII]}$, regions with higher surface brightness tend to have lower $W_{[CII]}$. This trend, observed at spatially resolved scales, can also influence the global $\alpha_{[CII]}$.

If a galaxy as a whole is characterized by a higher effective [CII] surface brightness, $\Sigma_{[CII],eff} = L_{[CII]}/(2\pi r^2_{e,[CII]})$, this implies that a large fraction of its ISM consists of bright patches with

[5] We ran `emcee` with ten random walkers exploring the parameter space for 50000 chain steps.

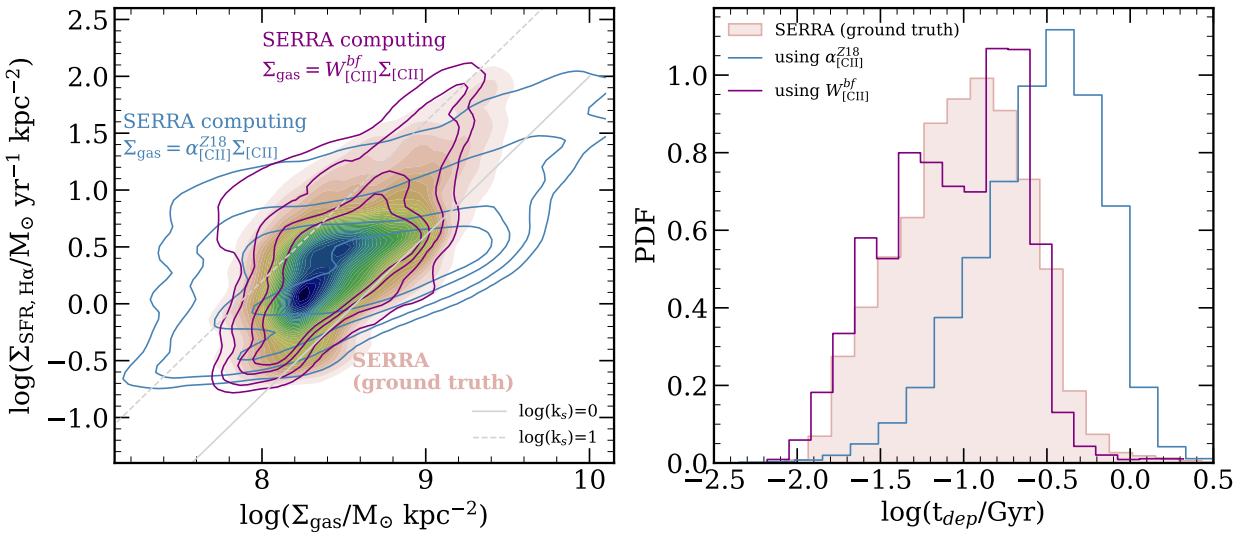

Fig. 7. Left: Spatially resolved KS relation considering $\approx 30 \times 30\,pc^2$ pixels drawn from the entire sample of SERRA galaxies (color-coded, ground truth). For each pixel the $\Sigma_{SFR,H\alpha}$ is derived from the Hα surface brightness using the Kennicutt (1998) relation, and the Σ_{gas} is taken from the simulation. For comparison, blue contours show the inferred location of the pixels on the KS plane assuming $\Sigma_{gas} = \alpha^{Z18}_{[CII]}\Sigma_{[CII]}$, namely adopting a constant Zanella et al. (2018) conversion factor to get the gas surface density from $\Sigma_{[CII]}$. The location in the KS plane found when using the best-fit spatially resolved conversion factor, $W_{[CII]}$ (Eq. (10)), is plotted in purple. Right: $L_{[CII]}$-weighted distribution of the depletion time (t_{dep}) in the SERRA pixels (shaded histogram), that inferred using $\alpha^{Z18}_{[CII]}$ to determine the Σ_{gas} (blue), and that obtained using the $W_{[CII]}$ from Eq. (10).

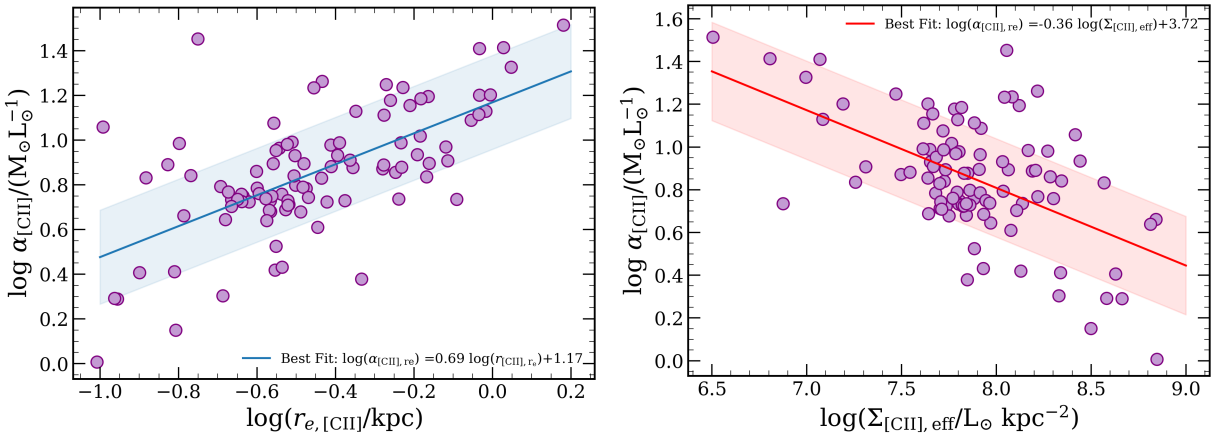

Fig. 8. Left: $\alpha_{[CII]}$ as a function of the [CII] half light radius for the sample considered in this work. Right: $\alpha_{[CII]}$ as a function of the [CII] effective surface brightness.

low $W_{[CII]}$. Since $\alpha_{[CII]}$ can be considered a [CII]-luminosity-weighted mean of $W_{[CII]}$, this suggests that more compact galaxies with higher $\Sigma_{[CII],eff}$ are also likely to have lower global $\alpha_{[CII]}$. Shedding light on this connection is key for interpreting unresolved observations and for accurately estimating gas masses from $L_{[CII]}$. From the $5 \times 5\,kpc^2$ maps we computed half-light radius ($r_{e,[CII]}$) of the [CII] emission to derive $\Sigma_{[CII],eff}$. We then calculated the conversion factor within $r_{e,[CII]}$ as $\alpha_{[CII]} = M_{gas,r_e}/L_{[CII],r_e}$. In Fig. 8 we present $\alpha_{[CII]}$ as a function of $r_{e,[CII]}$, and $\Sigma_{[CII],eff}$. We find, as expected, that galaxies with higher [CII] surface brightness–or equivalently, more compact galaxies with smaller $r_{e,[CII]}$–tend to exhibit lower values of $\alpha_{[CII]}$. This result highlights the impact of galaxy structure on the global conversion factor and suggests that $\Sigma_{[CII],eff}$, reminiscent of the local $\Sigma_{[CII]}$, is a good indicator of the conversion factor that should be used for a more precise estimate. We fit the following logarithmic relations:

$$\log(\alpha_{[CII]}/M_\odot\,L^{-1}_\odot) = A\,\log(r_{e,[CII]}/kpc) + C \quad (12)$$

and

$$\log(\alpha_{[CII]}/M_\odot\,L^{-1}_\odot) = A\,\log(\Sigma_{[CII],eff}/L_\odot\,kpc^{-2}) + C. \quad (13)$$

The parameters, along with their errors are listed in Table 1.

6. Conclusions

In this paper we have studied the [CII]-to-gas conversion factor in high-redshift galaxies ($z \approx 4$–9) extracted from the SERRA cosmological zoom-in simulation, both globally and down to spatially resolved scales. Our main findings can be summarized as follows:

– The mean global conversion factor in the SERRA sample is $\log(\alpha_{[CII]}/M_\odot\,L^{-1}_\odot) = 1.28$ ($\sigma = \pm 0.2$ dex). This is within the ranges derived in previous works, both observationally and with simulations. The $\alpha_{[CII]}$ anticorrelates with Z, and we provide a best-fit relation in Table 1. No significant correlation is found with redshift, stellar mass, or deviation from the MS.

Table 1. Best-fit relations for spatially resolved and global [CII] conversion factors.

Y (best fit)	X_1	X_2 (if present)	A	B	C	σ	Eq.
			Global relations				
$\log \alpha_{[CII]}$	$\log Z$	–	-0.39 ± 0.04	–	0.67 ± 0.06	0.14	[1]
$\log \alpha_{[CII]}$	$\log r_{e,[CII]}$	–	0.69 ± 0.08	–	1.17 ± 0.04	0.21	[12]
$\log \alpha_{[CII]}$	$\log \Sigma_{[CII],eff}$	–	-0.36 ± 0.06	–	3.7 ± 0.5	0.23	[13]
			Spatially resolved relations				
$\log W_{[CII]}$	$\log \Sigma_{[CII]}$	$\log Z$	$-0.355^{+0.003}_{-0.017}$	$-0.324^{+0.048}_{-0.004}$	$3.37^{+0.191}_{-0.026}$	0.18	[10]
$\log W_{[CII]}$	$\log \Sigma_{[CII]}$	–	-0.51 ± 0.001	–	4.93 ± 0.008	0.40	[11]

Notes. The fits follow the form $Y = AX_1 + BX_2 + C$ (for two-variable fits) or $Y = AX_1 + C$ (for single-variable fits). The units are as follows: $\alpha_{[CII]}$ in $[M_\odot\, L_\odot^{-1}]$, $W_{[CII]}$ in $[(M_\odot\, kpc^{-2})/(L_\odot\, kpc^{-2})]$, Z in $[Z_\odot]$, $\Sigma_{[CII]}$ in $[L_\odot\, kpc^{-2}]$, and $r_{e,[CII]}$ in [kpc]. We include the 1σ dispersion of residuals around every best-fit relation. The last column lists the reference equation in the main text of the paper.

- The spatially resolved conversion factor, $W_{[CII]}$, anticorrelates with n and Z. For $Z > 0.2\, Z_\odot$, the galaxy burstiness also modulates the $W_{[CII]}$, with bursty patches characterized by lower conversion factors. Since these regions are also characterized by high [CII] surface brightnesses, this leads to an inverse correlation between $W_{[CII]}$ and $\Sigma_{[CII]}$. In Table 1 we report the best-fit $W_{[CII]}$ as a function of Z and $\Sigma_{[CII]}$, which is a tight relation ($1\sigma = 0.18$ dex), and the $W_{[CII]}$ versus $\Sigma_{[CII]}$ only, which instead has a large dispersion ($1\sigma = 0.4$ dex). The second relation can be used to derive the cold gas surface density from spatially resolved [CII] maps if the information on Z is not available from other tracers.
- Adopting a fixed global $\alpha_{[CII]}$ to infer Σ_{gas} in the spatially resolved KS relation can lead to an artificially flat slope and to an overestimation of the depletion time by up to a factor of $\approx$4. This is because applying a uniform conversion factor leads to an overestimation of Σ_{gas} in bright $\Sigma_{[CII]}$ regions with $W_{[CII]}$ lower than the global $\alpha_{[CII]}$.
- The global $\alpha_{[CII]}$ is influenced by a galaxy's compactness. More compact galaxies (i.e., those with smaller $r_{e,[CII]}$ and higher $\Sigma_{[CII],eff}$) tend to be characterized by a lower global $\alpha_{[CII]}$. Our work hence suggests that the non-detection of [CII] in compact JWST-selected galaxies at $z > 10$ puts very strong constraints on the cold gas mass, indicating very short depletion times.

With this work we provide ready-to-use physically motivated relations (gathered in Table 1) that allow us to account for spatial variations in $\alpha_{[CII]}$. This is crucial for estimating gas masses and surface densities in both resolved and unresolved observations with ALMA in the EoR. We stress that using a physically motivated conversion factor can help in pinning down the right observation time required for following up in [CII] on JWST-selected galaxies, which are often metal-poor and relatively compact.

Acknowledgements. We thank the anonymous reviewer for their constructive comments that improved the quality of this work. LV acknowledges support from the INAF Minigrant "RISE: Resolving the ISM and Star formation in the Epoch of Reionization" (Ob. Fu. 1.05.24.07.01). We gratefully acknowledge the support of the Lorentz Center for the organization of the workshop "Synergistic ALMA+JWST view of the early Universe", held in December, 2024 in Leiden, during which this work was conceived. We acknowledge the CINECA award under the ISCRA initiative for the availability of high-performance computing resources and support from the Class B project SERRA HP10BPUZ8F (PI: Pallottini). We gratefully acknowledge the computational resources of the Center for High-Performance Computing (CHPC) at Scuola Normale Superiore. AZ acknowledges support from the INAF Minigrant "Clumps at cosmological distance: revealing their formation, nature, and evolution" (Ob. Fu. 1.05.23.04.01) and from the European Union – NextGeneration EU within PRIN 2022 project n. 20229YBSAN – "Globular clusters in cosmological simulations and in lensed fields: from their birth to the present epoch". CG, FP, and LV acknowledge funding from the ASI-INAF contract n. 2023-15-Q.0 CUP F83C25000230001 "Attività scientifiche propedeutiche alla partecipazione alla missione PRIMA del JPL/NASA". R.H.-C. thanks the Max Planck Society for support under the Partner Group project "The Baryon Cycle in Galaxies" between the Max Planck for Extraterrestrial Physics and the Universidad de Concepción. R.H-C. also gratefully acknowledge financial support from ANID - MILENIO - NCN2024_112 and ANID BASAL FB210003. We acknowledge use of Astropy (Astropy Collaboration 2018), Matplotlib (Hunter 2007), SciPy (Virtanen et al. 2020), Seaborn (Waskom 2021), Pandas (The Pandas Development Team 2024).

References

Accurso, G., Saintonge, A., Catinella, B., et al. 2017, MNRAS, 470, 4750
Adams, N. J., Conselice, C. J., Austin, D., et al. 2024, ApJ, 965, 169
Algera, H., Rowland, L., Stefanon, M., et al. 2025, arXiv e-prints [arXiv:2501.10508]
Arrabal Haro, P., Dickinson, M., Finkelstein, S. L., et al. 2023, ApJ, 951, L22
Asplund, M., Grevesse, N., Sauval, A. J., & Scott, P. 2009, ARA&A, 47, 481
Astropy Collaboration (Price-Whelan, A. M., et al.) 2018, AJ, 156, 123
Béthermin, M., Fudamoto, Y., Ginolfi, M., et al. 2020, A&A, 643, A2
Béthermin, M., Accard, C., Guillaume, C., et al. 2023, A&A, 680, L8
Bolatto, A. D., Wolfire, M., & Leroy, A. K. 2013, ARA&A, 51, 207
Bouwens, R. J., Smit, R., Schouws, S., et al. 2022, ApJ, 931, 160
Bovino, S., Grassi, T., Capelo, P. R., Schleicher, D. R. G., & Banerjee, R. 2016, A&A, 590, A15
Capak, P. L., Carilli, C., Jones, G., et al. 2015, Nature, 522, 455
Carniani, S., Maiolino, R., Amorin, R., et al. 2018, MNRAS, 478, 1170
Carniani, S., Hainline, K., D'Eugenio, F., et al. 2024, Nature, 633, 318
Casavecchia, B., Maio, U., Péroux, C., & Ciardi, B. 2025, A&A, 693, A119
Castellano, M., Fontana, A., Treu, T., et al. 2023, ApJ, 948, L14
Cole, J. W., Papovich, C., Finkelstein, S. L., et al. 2025, ApJ, 979, 193
Croxall, K. V., Smith, J. D., Pellegrini, E., et al. 2017, ApJ, 845, 96
de los Reyes, M., & Kennicutt, R. C. 2019, ApJ, 872, 16
Decataldo, D., Ferrara, A., Pallottini, A., Gallerani, S., & Vallini, L. 2017, MNRAS, 471, 4476
Dekel, A., Sarkar, K. C., Birnboim, Y., Mandelker, N., & Li, Z. 2023, MNRAS, 523, 3201
Dessauges-Zavadsky, M., Ginolfi, M., Pozzi, F., et al. 2020, A&A, 643, A5
Donnan, C. T., McLure, R. J., Dunlop, J. S., et al. 2024, MNRAS, 533, 3222
Ebagezio, S., Seifried, D., Walch, S., et al. 2023, MNRAS, 525, 5631
Faisst, A. L., Schaerer, D., Lemaux, B. C., et al. 2020, ApJS, 247, 61
Federrath, C., & Klessen, R. S. 2013, ApJ, 763, 51
Ferland, G. J., Chatzikos, M., Guzmán, F., et al. 2017, Rev. Mex. Astron. Astrofis., 53, 385
Ferrara, A. 2024, A&A, 684, A207
Ferrara, A., Vallini, L., Pallottini, A., et al. 2019, MNRAS, 489, 1
Ferrara, A., Pallottini, A., & Dayal, P. 2023, MNRAS, 522, 3986
Finkelstein, S. L., Bagley, M., Song, M., et al. 2022, ApJ, 928, 52
Finkelstein, S. L., Leung, G. C. K., Bagley, M. B., et al. 2024, ApJ, 969, L2
Foreman-Mackey, D., Conley, A., Meierjurgen Farr, W., et al. 2013, Astrophysics Source Code Library [record ascl:1303.002]
Fudamoto, Y., Oesch, P. A., Walter, F., et al. 2024, MNRAS, 530, 340
Gelli, V., Pallottini, A., Salvadori, S., et al. 2025, ApJ, 985, 126
Girichidis, P., Konstandin, L., Whitworth, A. P., & Klessen, R. S. 2014, ApJ, 781, 91
Glazer, K., Bradač, M., Sanders, R. L., et al. 2024, MNRAS, 531, 945

Grassi, T., Bovino, S., Schleicher, D. R. G., et al. 2014, MNRAS, 439, 2386
Gurman, A., Hu, C.-Y., Sternberg, A., & van Dishoeck, E. F. 2024, ApJ, 965, 179
Habing, H. J. 1968, Bull. Astron. Inst. Netherlands, 19, 421
Hahn, O., & Abel, T. 2011, MNRAS, 415, 2101
Heiderman, A., Evans, N. J., II, Allen, L. E., Huard, T., & Heyer, M. 2010, ApJ, 723, 1019
Heintz, K. E., Watson, D., Oesch, P. A., Narayanan, D., & Madden, S. C. 2021, ApJ, 922, 147
Herrera-Camus, R., Förster Schreiber, N., Genzel, R., et al. 2021, A&A, 649, A31
Herrera-Camus, R., González-López, J., Förster Schreiber, N., et al. 2025, A&A, 669, A80
Hunter, J. D. 2007, Comput. Sci. Eng., 9, 90
Hutter, A., Cueto, E. R., Dayal, P., et al. 2025, A&A, 694, A254
Ikeda, R., Tadaki, K.-I., Mitsuhashi, I., et al. 2025, A&A, 693, A237
Inami, H., Algera, H., Schouws, S., et al. 2022, MNRAS, 515, 3126
Jones, G. C., Übler, H., Perna, M., et al. 2024, A&A, 682, A122
Kaasinen, M., Venemans, B., Harrington, K. C., et al. 2024, A&A, 684, A33
Katz, H., Kimm, T., Sijacki, D., & Haehnelt, M. G. 2017, MNRAS, 468, 4831
Katz, H., Rosdahl, J., Kimm, T., et al. 2022, MNRAS, 510, 5603
Kennicutt, R. C. 1998, ApJ, 498, 541
Khusanova, Y., Bethermin, M., Le Fèvre, O., et al. 2021, A&A, 649, A152
Knudsen, K. K., Richard, J., Kneib, J.-P., et al. 2016, MNRAS, 462, L6
Kohandel, M., Pallottini, A., Ferrara, A., et al. 2020, MNRAS, 499, 1250
Kohandel, M., Pallottini, A., Ferrara, A., et al. 2024, A&A, 685, A72
Kovačić, I., Barnes, A. T., Bigiel, F., et al. 2025, A&A, 694, A87
Lagache, G., Cousin, M., & Chatzikos, M. 2018, A&A, 609, A130
Leitherer, C., Schaerer, D., Goldader, J. D., et al. 1999, ApJS, 123, 3
Leroy, A. K., Sun, J., Meidt, S., et al. 2025, ApJ, 985, 14
Li, Z., Dekel, A., Sarkar, K. C., et al. 2024, A&A, 690, A108
Lupi, A., & Bovino, S. 2020, MNRAS, 492, 2818
Lupi, A., Pallottini, A., Ferrara, A., et al. 2020, MNRAS, 496, 5160
Mac Low, M.-M., & Ferrara, A. 1999, ApJ, 513, 142
Madden, S. C., Cormier, D., Hony, S., et al. 2020, A&A, 643, A141
Maiolino, R., Carniani, S., Fontana, A., et al. 2015, MNRAS, 452, 54
Matteri, A., Pallottini, A., & Ferrara, A. 2025a, A&A, 697, A65
Matteri, A., Ferrara, A., & Pallottini, A. 2025b, A&A, submitted [arXiv:2503.18850]
Matthee, J., Sobral, D., Boogaard, L. A., et al. 2019, ApJ, 881, 124
Mirocha, J., & Furlanetto, S. R. 2023, MNRAS, 519, 843
Mitsuhashi, I., Zavala, J. A., Bakx, T. J. L. C., et al. 2025, arXiv e-prints [arXiv:2501.19384]
Naidu, R. P., Oesch, P. A., van Dokkum, P., et al. 2022, ApJ, 940, L14
Narayanan, D., Krumholz, M., Ostriker, E. C., & Hernquist, L. 2011, MNRAS, 418, 664
Nikolić, I., Mesinger, A., Davies, J. E., & Prelogović, D. 2024, A&A, 692, A142
Olsen, K., Greve, T. R., Narayanan, D., et al. 2017, ApJ, 846, 105
Padmanabhan, H., & Loeb, A. 2023, ApJ, 953, L4
Pallottini, A., & Ferrara, A. 2023, A&A, 677, L4
Pallottini, A., Ferrara, A., Gallerani, S., et al. 2017a, MNRAS, 465, 2540
Pallottini, A., Ferrara, A., Bovino, S., et al. 2017b, MNRAS, 471, 4128
Pallottini, A., Ferrara, A., Decataldo, D., et al. 2019, MNRAS, 487, 1689
Pallottini, A., Ferrara, A., Gallerani, S., et al. 2022, MNRAS, 513, 5621
Pallottini, A., Ferrara, A., Gallerani, S., et al. 2025, A&A, 699, A6
Pineda, J. L., Langer, W. D., & Goldsmith, P. F. 2014, A&A, 570, A121
Posses, A. C., Aravena, M., González-López, J., et al. 2023, A&A, 669, A46
Ramambason, L., Lebouteiller, V., Madden, S. C., et al. 2024, A&A, 681, A14
Rémy-Ruyer, A., Madden, S. C., Galliano, F., et al. 2014, A&A, 563, A31
Rizzo, F., Vegetti, S., Fraternali, F., Stacey, H. R., & Powell, D. 2021, MNRAS, 507, 3952
Rizzo, F., Kohandel, M., Pallottini, A., et al. 2022, A&A, 667, A5
Rosdahl, J., Blaizot, J., Aubert, D., Stranex, T., & Teyssier, R. 2013, MNRAS, 436, 2188
Salvestrini, F., Feruglio, C., Tripodi, R., et al. 2025, A&A, 695, A23
Sandstrom, K. M., Leroy, A. K., Walter, F., et al. 2013, ApJ, 777, 5
Schimek, A., Decataldo, D., Shen, S., et al. 2024, A&A, 682, A98
Schmidt, M. 1959, ApJ, 129, 243
Schouws, S., Bouwens, R. J., Algera, H., et al. 2025, arXiv e-prints [arXiv:2502.01610]
Solimano, M., González-López, J., Aravena, M., et al. 2024, A&A, 689, A145
Sommovigo, L., Ferrara, A., Carniani, S., et al. 2021, MNRAS, 503, 4878
Sun, G., Faucher-Giguère, C.-A., Hayward, C. C., et al. 2023, ApJ, 955, L35
Tacchella, S., Johnson, B. D., Robertson, B. E., et al. 2023, MNRAS, 522, 6236
Teyssier, R. 2002, A&A, 385, 337
The Pandas Development Team 2024, https://doi.org/10.5281/zenodo.10697587
Tielens, A. G. G. M. 2005, The Physics and Chemistry of the Interstellar Medium (Cambridge: Cambridge University Press)
Topping, M. W., Stark, D. P., Endsley, R., et al. 2022, MNRAS, 516, 975
Trinca, A., Schneider, R., Valiante, R., et al. 2024, MNRAS, 529, 3563
Tripodi, R., D'Eugenio, F., Maiolino, R., et al. 2024, A&A, 692, A184
Übler, H., Maiolino, R., Curtis-Lake, E., et al. 2023, A&A, 677, A145
Vallini, L., Gallerani, S., Ferrara, A., Pallottini, A., & Yue, B. 2015, ApJ, 813, 36
Vallini, L., Pallottini, A., Ferrara, A., et al. 2018, MNRAS, 473, 271
Vallini, L., Witstok, J., Sommovigo, L., et al. 2024, MNRAS, 527, 10
Venturi, G., Carniani, S., Parlanti, E., et al. 2024, A&A, 691, A19
Veraldi, E., Vallini, L., Pozzi, F., et al. 2025, A&A, 693, A34
Virtanen, P., Gommers, R., Oliphant, T. E., et al. 2020, Nat. Meth., 17, 261
Vizgan, D., Greve, T. R., Olsen, K. P., et al. 2022, ApJ, 929, 92
Waskom, M. L. 2021, J. Open Source Softw., 6, 3021
Weingartner, J. C., & Draine, B. T. 2001, ApJ, 548, 296
Witstok, J., Smit, R., Maiolino, R., et al. 2022, MNRAS, 515, 1751
Witstok, J., Maiolino, R., Smit, R., et al. 2025, MNRAS, 536, 27
Wolfire, M. G., McKee, C. F., Hollenbach, D., & Tielens, A. G. G. M. 2003, ApJ, 587, 278
Wolfire, M. G., Hollenbach, D., & McKee, C. F. 2010, ApJ, 716, 1191
Wolfire, M. G., Vallini, L., & Chevance, M. 2022, ARA&A, 60, 247
Zanella, A., Daddi, E., Magdis, G., et al. 2018, MNRAS, 481, 1976
Zhao, Y., Liu, J., Zhang, Z.-Y., & Bisbas, T. G. 2024, ApJ, 977, 46

Appendix A: Global trends in SERRA

In Fig. A.1 we report the scatter plot between $\alpha_{[CII]}$ and redshift, stellar mass, and deviation with respect to the MS.

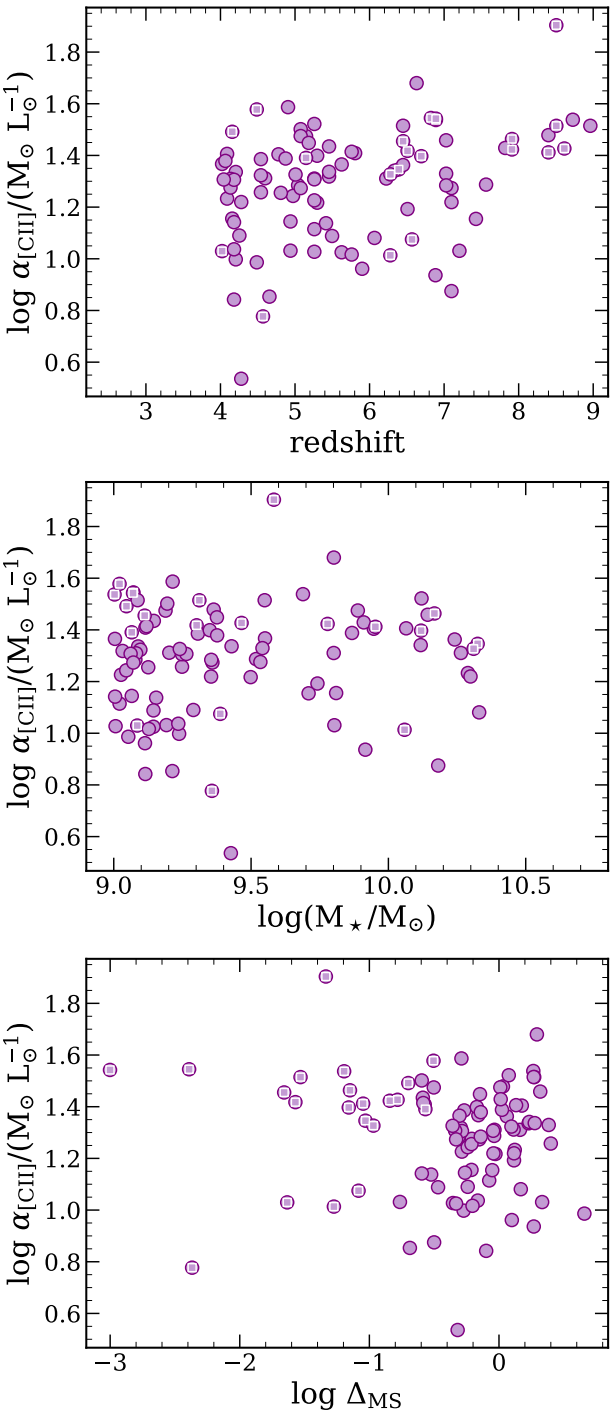

Fig. A.1. Global $\alpha_{[CII]}$ vs. redshift (top panel), stellar mass (middle panel), and deviation from the MS (bottom panel) for the SERRA sample. We adopt the MS from Cole et al. (2025) in the corresponding redshift bin of each SERRA galaxy. The symbol meanings are the same as in Fig. 1.